

Performance assessment of grid-forming and grid-following converter-interfaced battery energy storage systems on frequency regulation in low-inertia power grids[☆]

Yihui Zuo^{a,*}, Zhao Yuan^a, Fabrizio Sossan^b, Antonio Zecchino^a, Rachid Cherkaoui^a, Mario Paolone^a

^a École Polytechnique Fédérale de Lausanne EPFL, Lausanne, Switzerland

^b Center for Processes, Renewable energies and Energy systems, MINES ParisTech - PSL, France

ARTICLE INFO

Article history:

Received 24 December 2020

Received in revised form 7 March 2021

Accepted 13 May 2021

Available online 20 May 2021

Keywords:

Battery energy storage

Converter control

Grid-forming

Grid-following

Frequency containment

Unit commitment

Dynamic simulation

ABSTRACT

Power systems with large shares of converter-interfaced renewables may be characterized by low grid inertia due to the lack of frequency containment provided by synchronous generators. Battery energy storage systems (BESSs), which can adjust their power output at much steeper ramping than conventional generation, are promising assets to restore suitable frequency regulation capacity levels. BESSs are typically connected to the grid with a power converter, which can be operated in either grid-forming or grid-following modes. This paper quantitatively assesses the impact of large-scale BESSs on the frequency containment of low inertia power grid and compares the performance of grid-forming and grid-following control modes. Numerical results are provided considering a detailed dynamic model of the IEEE 39-bus system where fully characterized models of stochastic demand and generation are taken into account. In order to assess the performance of the BESS control modes in a practical operative context, daily long simulations are considered where reserve levels for frequency containment and restoration are allocated considering the current practice of a transmission system operator in Europe. Numerical analyses on various metrics applied to grid frequency show that grid-forming outperforms grid-following converter control mode.

© 2021 The Authors. Published by Elsevier Ltd. This is an open access article under the CC BY license (<http://creativecommons.org/licenses/by/4.0/>).

1. Introduction

Power systems are going through the transition from a significant share of conventional power generation to massive renewable resources interfaced by power electronics. Renewable power generation levels larger than 15% of the overall annual electricity generation is now a reality for several European countries [1]. In Australia, the total wind and solar capacity is rapidly increasing and has reached 20% in the National Electricity Market (NEM) [2]. In the United States, the installed capacity of renewable generation has reached 20% of the total generation capacity at the national level, with peaks over 40% in the grids of the Western Electricity Coordinating Council (WECC) and California Independent System Operator (CAISO) [3].

As broadly acknowledged in the power systems community, a large deployment of converter-interfaced generation determines

lower grid inertia levels and calls for a review of frequency containment concepts and the identification of assets capable to maintain the power balance. In fact, some power systems are already facing this control challenge. The Australian Energy Market Operator (AEMO) has observed that lower frequency containment provided by generators results in a lack of effective control of frequency under normal operating conditions [4]. Consequently, the lack of consistent and certain frequency containment delivered from conventional power plants has impacted AEMO's ability to effectively plan the system reserves. CAISO has also observed a progressive deterioration of its frequency containment and restoration performance: the frequency response measure (FRM¹) has steadily decreased from 263 MW/0.1 Hz in 2012 to 141 MW/0.1 Hz in 2016 [5].

In this context, converter-interfaced battery energy storage systems (BESSs) are advocated as a potential solution for grid frequency regulation (e.g., [6]) thanks to their large ramping

[☆] This work is supported by OSMOSE project. The project has received funding from the European Union's Horizon 2020 Research and Innovation Program under Grant 773406.

* Corresponding author.

E-mail address: yihui.zuo@epfl.ch (Y. Zuo).

¹ The FRM, calculated in resources of MW/0.1 Hz, is the change in net actual interchange on the inter-tie lines between the pre-event period (point A) and the stabilizing period after the event (point B) per 0.1 Hz of the frequency event measured between the those two points.

rates, high round-trip efficiency and commercial availability [7]. Recently installed large BESSs, like the 100 MW/129 MWh unit of the Hornsdale Power Reserve (HPR) in Australia [8] and the 300 MW/1200 MWh unit at Moss Landing in California [9], have shown the applicability of this technology in practical contexts.

As BESSs can provide significant value to both frequency containment and restoration services, quantitatively evaluating their performance is of fundamental importance for transmission grid operators. To the best of the Authors' knowledge, very few researches have attempted to quantitatively assess the impact of BESS converter control strategies on the grid frequency using a detailed model of a realistic low-inertia power system. The work in [10] studies the impact of a BESS on grid frequency transients using a dynamic model of a simple low-inertia grid. However, the BESS is modelled as an ideal power source and falls short of capturing the dynamic interactions between the converter and the grid. In [11], BESS's and grid's dynamic models are used to show that the BESS can reduce frequency oscillations after a disturbance. Nevertheless, this work only assesses the post-disturbance performance of BESS under a single system operation point. Yet, [10] and [11] have not considered the possible influences of different converter controls. In this context, this paper contributes to the current state of the art by explicitly modelling the BESS dynamics and comparing grid-forming and grid-following control strategies.

The simulation framework used in this paper is based on the one proposed in [12]. It consists of a detailed dynamic model of the low-inertia 39-bus power system hosting conventional and renewable power generation and converter-interfaced BESS. In this paper, this model is coupled with a day-ahead schedule layer so as to statistically evaluate the daily system frequency containment via 24-hour long time-domain simulations. In order to reproduce a realistic grid operative scenario for the numerical analyses, power reserves for frequency containment and restoration are allocated following the procedure adopted by a transmission system operator (TSO). This stage, also described in the paper, leverages a unit commitment formulation fed by forecasts of renewable generation and demand computed with state-of-the-art methods.

The contributions of this paper are listed here below.

- (1) Propose a comprehensive benchmark framework, that comprises a day-ahead schedule layer with procedures nowadays adopted by TSOs and a day-long real-time operation stage that provides a way to assess the frequency containment performance of power systems under daily operation.
- (2) A comprehensive simulation model of a low-inertia power grid that includes detailed dynamic models of all the devices in order to obtain the dynamics that are not captured by simplified models. Particularly, we consider the dynamic interactions between the low-inertia power grid and the converter-based BESS, and the closed-loop dynamics between the converter and the battery DC voltage model.
- (3) Quantitative comparison of the impact of grid-forming versus grid-following converter-interfaced BESS on the system frequency containment via suitably-defined frequency metrics.

The rest of the paper is structured as follows. Section 2 presents the state of the art on converters' control. Section 3 describes the adopted frequency control strategies. Section 4 describes the simulation framework and power reserves allocation. Section 5 illustrates the study cases and simulation results, and Section 6 concludes the paper.

2. State of the art on converters' control

There are generally two main approaches to achieve the power control for power converter-interfaced units: *grid-following* and *grid-forming* controls [13–15]. Here below we recall the definitions of grid-following and grid-forming controls proposed in [13].

In a grid-following converter, the current injected by the converter is controlled with a specific phase displacement from the grid voltage at the point of common coupling (PCC). As a consequence, the knowledge of the fundamental frequency phasor of the grid voltage is needed at any time for the correct calculation of the converter's reference current, whose amplitude and angle with respect to the grid voltage phasor are properly modified by outer control loops so as to inject the required amount of active and reactive power or control the RMS voltage.

In a grid-forming unit, the magnitude and angle of the voltage at the PCC are controlled. As a consequence, the knowledge of the fundamental frequency phasor of the grid voltage at the point of connection is not strictly necessary. Depending on the characteristics of the network to which the converter is connected, an isolated system or a slack bus, it is possible by means of additional outer loops to adapt the injected instantaneous active and reactive power also to provide voltage and frequency support. In an isolated system, a grid-forming unit could behave itself like a slack-bus. When connected with other power sources, through an inductive line, the grid-forming converter is controlling the active power by the modification of the angle. The voltage magnitude is independent of the active power control.

In contrast to the grid-following control whose concept has been widely accepted, several variants of control laws allowing the grid-forming capability have been recently proposed [16–18]. Some new controllers have been proposed to make the converter behave like synchronous machine, e.g. Virtual Synchronous Generator (VSG) [19–21], Virtual Synchronous Machine (VSM) [22, 23], VISMA [24], Synchronverter [25,26], droop-based control [27, 28]. Some of those controllers (e.g., VSG and VSM) use a Phase Locked-Loop (PLL) to decouple the power control from frequency control capability, while the droop-based controls are PLL-free. The benefit of using PLL-free controls is to avoid the stability issues caused by PLL and possibly the interaction between the PLL and power controller [29]. Another recently introduced grid-forming control law is the Virtual Oscillator (VOC) [30,31]. It provides a way to synchronize and control the converter by acting as a non-linear oscillator. This control may be more advantageous in case of voltage unbalance and distortion due to its non-linear characteristics. However, its robustness of interacting with the grids, that comprise various generation resources (i.e., the mix of synchronous generations and power-electronics devices interfaced generations), has not yet been properly studied and may be the subject of future studies. In this context, the droop-based PLL-free grid-forming control proposed in [28] is considered in this paper as it has been proved to be robust on a wide range of short circuit ratio (i.e., 1.2 to 20) as well as under contingency analysis in low-inertia power grids [12].

3. Implemented frequency control strategies

3.1. Power converter controls

3.1.1. PLL-free grid-forming converter control

A grid-forming converter controls the magnitude and angle of the voltage at its terminals, thus linking the active power exchange with the angle difference between the modulated voltage and the grid voltage at PCC. In this context, the estimate of grid voltage angle is necessary and can be achieved in two ways: by

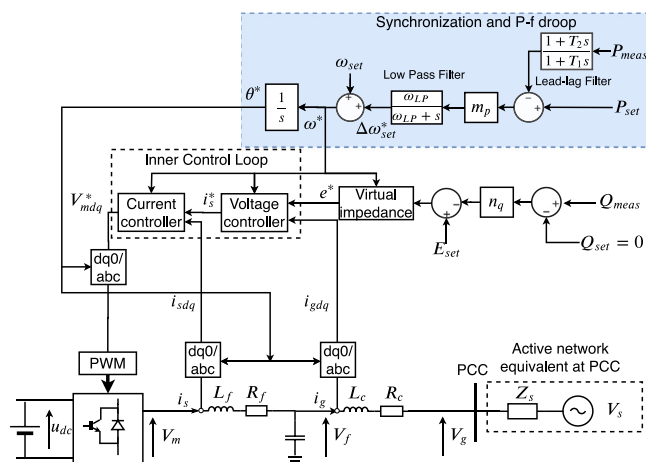


Fig. 1. PLL-free grid-forming converter.

using a PLL or directly linking the active power exchange to the angle difference between the grid and the modulated voltages to create a PLL-free controller.

We opt for the PLL-free grid-forming control proposed in [28]. This control layout, highlighted in blue Fig. 1, is an effective and simple scheme that allows the converter to synchronize with the grid and provide the frequency containment. Specifically, the frequency droop coefficient m_p corresponds to the active power-frequency p - f droop coefficient. The reactive power compensation with droop n_q adjusts the voltage magnitude reference according to the difference between actual reactive power output and the reference reactive power. A first-order low-pass filter with cut-off frequency ω_{LP} is added to avoid fast frequency variations imposed by the control of the converter's terminal and filter out the power measurements noise; a lead-lag filter with time constants T_1 and T_2 is applied to the power measurements to improve the converter dynamics [32]. It is worth noting that in the adopted grid-forming control, a virtual impedance is included in order to keep the control as it was proposed in the original MIGRATE project report [28]. However, the virtual impedance is only activated to limit the current under over-current condition (e.g. short-circuits). Under the normal operating conditions we tested, it is not activated.

3.1.2. Grid-following converter operated with grid-supporting mode

The grid-forming control adjusts the modulated voltage with respect to the grid voltage at PCC, whereas the grid-following control adjusts the injected power with respect to the grid voltage at the PCC. As shown in Fig. 2, the grid-following converter controls the values of active and reactive power by controlling the amplitude and phase of the injected current with respect to the grid-voltage at the PCC. In this case, a three-phase PLL is required to estimate the fundamental frequency phasor of the grid voltage, so as to generate the instantaneous value of the current reference and, eventually, the voltage reference. In this regard, the active and reactive power are controlled independently.

The grid-following converter is operated with grid-supporting mode by adding higher-level frequency and voltage droop regulators. The active power is regulated according to the f - p control gain $K_{f-p}^{following}$, as the frequency deviates from the reference value. The reactive power is regulated according to the v - q control gain $K_{v-q}^{following}$, as the difference between the measured voltage and the voltage reference exceeds the dead-band of ΔV_{tr} . Fig. 3 illustrates the PLL with moving average filter (MAF) from [33] used for tracking the fundamental phasor of grid voltage at the PCC. It consists of a phase detector, a loop filter and a voltage controlled

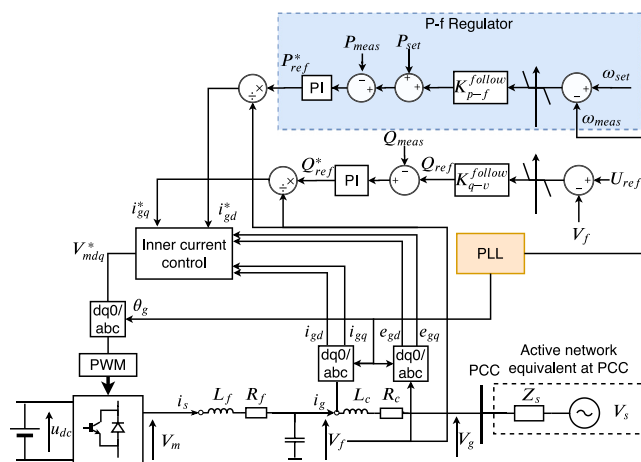


Fig. 2. Grid-following converter with grid-supporting mode.

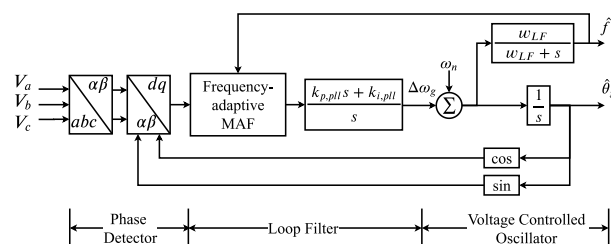


Fig. 3. PLL implemented in grid-following converter with grid-supporting mode.

oscillator. The loop filter includes a frequency-adaptive MAF and a PI controller so as to enhance the PLL's filtering capability [34]. The time window length, T_{wd} , of the frequency-adaptive MAF is adjusted online according the frequency variation as $T_{wd} = 1/\hat{f}_g$, where \hat{f}_g is the PLL estimated frequency. The parameter w_{LF} is the cut-off frequency of the low-pass filter applied to reduce the oscillation of \hat{f}_g , which is used by both the frequency-adaptive MAF and upper-level frequency regulator.

3.2. Frequency controls in synchronous generators

3.2.1. Frequency containment and restoration regulation

The synchronous generators provide both frequency containment and frequency restoration, as shown in Fig. 4. The parameter R_p is the static droop coefficient for frequency containment, T_s is the integration time constant for the frequency restoration regulation, w_{ref} is reference frequency (i.e., nominal frequency), w_{meas} is measured actual frequency, P_{set} is the power set-point scheduled for the generator, and P_{ref} is the power reference for the turbine-governor system.

3.2.2. Hydraulic turbine and governor system

As it will be detailed in Section 4.5, the low-inertia 39-bus power grid includes only hydropower plants, being thermal generation replaced by wind power [12]. The adopted governing system for hydropower plants is shown in Fig. 5 and is from [35]. It consists of a PI governor, a servomotor, and a non-linear turbine-water column model that accounts for the effects of varying flow on the effective water starting time. Parameters $k_{p,gov}$ and $k_{i,gov}$ are the proportional and integral gains of the PI governor, k_a and T_a are the gain and time constant of the servomotor, and T_w the water starting time of the hydro water column.

The values of the parameters presented in this section are listed in [Appendix](#).

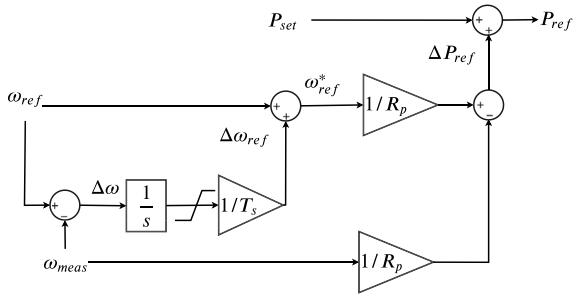


Fig. 4. Diagram of the synchronous generator frequency containment and restoration regulators.

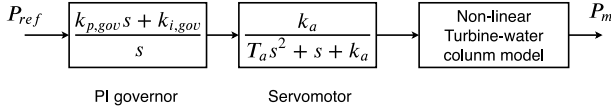


Fig. 5. Diagram of the hydro turbine-governing system.

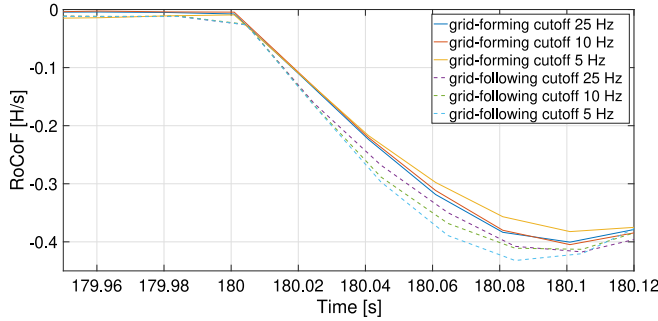


Fig. 6. Post-contingency RoCoF for p - f droop coefficients (f - p control gains) 2% (225 MW/Hz).

3.3. Sensitivity analysis

We conducted a sensitivity analysis of the system frequency response with respect to the critical converter control parameters. Two critical controls parameters that have a major impact on the control of the converters are studied: the p - f droop coefficient (f - p control gain) and the cut-off frequency of the low-pass filter.² The sensitivity of the system frequency response to these parameters is studied on the same low-inertia 39-bus power grid presented in Section 4.5. To excite the converter control response, we simulated a large contingency: the outage of G4 (i.e., tripping of 300 MW generation power).

In order to be in line with the p - f droop coefficients (f - p control gains) adopted in the 24-hour long simulation cases in , the same p - f droop coefficients (f - p control gains) are selected in the contingency tests, namely, 2% (225 MW/Hz) and 1% (450 MW/Hz). As for the cut-off frequency of the low-pass filters, it should be tuned in a range that is wide enough while also insuring controls' stability [28,34]. To this end, the cut-off frequency is tuned in the range from 1/2 to 1/10 of the nominal frequency, i.e., the selected values are 25 Hz, 10 Hz and 5 Hz, respectively.

Figs. 6 and 7 show the system post-contingency Rate-of-Change-of-Frequency (RoCoF) for the p - f droop coefficients 2% (f - p control gain 225 MW/Hz) and 1% (f - p control gain 450

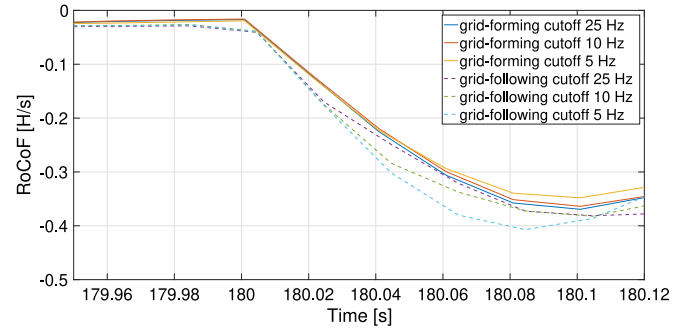


Fig. 7. Post-contingency RoCoF for p - f droop coefficients (f - p control gains) 1% (450 MW/Hz).

MW/Hz), respectively. The RoCoF is computed as the discrete first time derivative of the system frequency³ with time difference $\Delta t = 20$ ms. The fact that the RoCoF instead of frequency is used as an index for comparing different cases, is to better highlight the differences in post-contingency system frequency performance. On one hand, for both grid-forming and grid-following controls, the case with lower p - f droop coefficient 1% (higher f - p control gain 450 MW/Hz) exhibits higher RoCoF than the case with higher p - f droop coefficient 2% (lower f - p control gain 225 MW/Hz). This is consistent with the expectation that the lower p - f droop coefficient (higher f - p control gain) leads to larger amount of active power injected by the converter into the power grid, thereby allowing improved system frequency containment. On the other hand, with the same p - f droop coefficient (f - p control gain), the cut-off frequency of the low-pass filter also affects the performance of the converter controls. For the grid-forming control, reducing the cut-off frequency increases the post-contingency RoCoF, whereas for the grid-following control, reducing the cut-off frequency decreases post-contingency RoCoF. In the grid-forming control, the equivalent inertia constant is represented by the term $\frac{1}{2m_p\omega_{LP}}$ [28], whereby the frequency is better contained with lower ω_{LP} as it corresponds to higher equivalent inertia. In the grid-following control, the higher ω_{LP} for the low-pass filter in PLL allows to capture faster frequency dynamics, therefore enabling the converter to react faster to the frequency decreasing after the contingency.

In this respect, the cut-off frequency of the low-pass filter that allows the best converter contribution to the system frequency containment has been adopted, i.e., 5 Hz for the grid-forming control and 25 Hz for the grid-following control. From Figs. 6 and 7 it can be seen that, overall, the grid-forming control outperforms the grid-following control for both the cases with p - f droop coefficients 2% and 1% (f - p control gains 225 MW/Hz and 450 MW/Hz). Nevertheless, in the condition where the grid-forming control adopts an unfavourable cut-off frequency while the grid-following control uses an advantageous one, the grid-forming converter may not outperform the grid-following converter.

4. Simulation framework

4.1. Framework structure

The proposed simulation framework has two layers: real-time simulations and a scheduling stage. The former is used to evaluate the performance of the converter controllers by analysing the whole grid dynamic behaviour. The latter allows to size power

² In the grid-forming control, the low-pass filter is inside the synchronization and p - f droop layer. In the grid-following control, the low-pass filter is inside the PLL (see Fig. 3).

³ For all the cases, we consider the rotor speed of the same generator as system frequency.

reserve requirements and reproduce realistic operative scenarios for the real-time simulations. Fig. 8 illustrates the overall simulation process, where L and W denote measurements of power demand and wind generation, respectively. The process starts with dividing the measurements into two subsets, one for training the forecasting and model, and one to feed the real-time simulations. Measurements and forecasts are discussed in 4.2.

Accordingly, the demand profile denoted by the sequence $L = \{l_1, l_2, \dots, l_n\}$ is separated as $L_1 = \{\tilde{l}_1, \tilde{l}_2, \dots, \tilde{l}_{n-24}\}$ and $L_2 = \{l_{n-23}, l_{n-22}, \dots, l_n\}$, and the wind generation profile denoted by the sequence $W = \{w_1, w_2, \dots, w_m\}$ is separated as $W_1 = \{\tilde{w}_1, \tilde{w}_2, \dots, \tilde{w}_{m-24}\}$ and $W_2 = \{w_{m-23}, w_{m-22}, \dots, w_m\}$.⁴ L_2 and W_2 are directly applied to the RTS to be reproduced in the day-long simulations. At the day-head schedule layer, L_1 and W_1 are sent to the forecasting models (described in Section 4.2) to obtain the demand and wind generation forecasting results, which are then used to compute the frequency restoration reserve, with the procedure described in Section 4.3. Additionally, L_1 is also used for computing the frequency containment reserve as is considered as 10% of peak load (described in Section 4.3). Then, a unit commitment model determines an optimal hourly generation and reserve schedule accounting for the demand and wind generation forecasting results, the frequency containment and restoration reserves, as well as the power network and operational constraints (detailed in Section 4.4). Eventually, the RTS executes simulations of the dynamic models of the low-inertia 39-bus power grids which are implemented with the realistic demand and wind generation profiles (i.e., L_2 and W_2) and the energy generation and reserve schedules provided by the unit commitment model.

It is worth to note that, in the low-inertia 39-bus power grid, all the devices (including type-III wind power plants, synchronous generators, converter-interfaced BESS and frequency and voltage-dependent dynamic loads) are fully modelled in time domain to make the simulations as close as possible to the realistic scenario. Moreover, the converter is modelled by switching devices (i.e., IGBT and Diode) in order to adequately capture the dynamics due to the interaction between the grid-forming/grid-following converter and the system frequency. In view of the high computational complexity and the microsecond-scale time-integration step required by the high sampling frequency devices (i.e., Pulse Width Modulation (PWM) generator of the converter and Phase Measurement Units (PMUs)), we choose to adopt a real-time simulation platform. All dynamic models used for the simulations are built in MATLAB/Simulink and executed in an OPAL-RT eMEGAsim real-time simulator. For the sake of reproducibility, all the models are open-source available online [36].

The demand and wind generation forecasting, the system reserves allocation, the unit commitment model and the dynamic models of the low-inertia 39-bus power grid are described in the following sub-sections.

4.2. Measurements and forecasting

Although it is not a specific contribution of this paper, forecasting stochastic generation and demand is a necessary element of the process and thus briefly discussed here below.

⁴ It should be noted that $l_i = \{l_{i,1}, l_{i,2}, \dots, l_{i,3600}\}$ is the 1-s resolution demand set for hour i and \tilde{l}_i is the average demand of hour i . w_i and \tilde{w}_i are likewise the 1-s resolution wind generation set and the average wind generation for hour i , respectively.

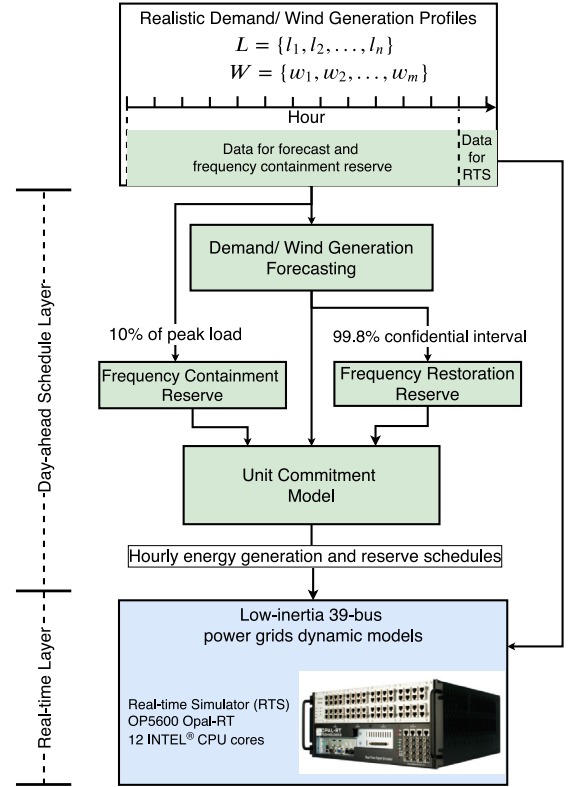


Fig. 8. Simulation framework.

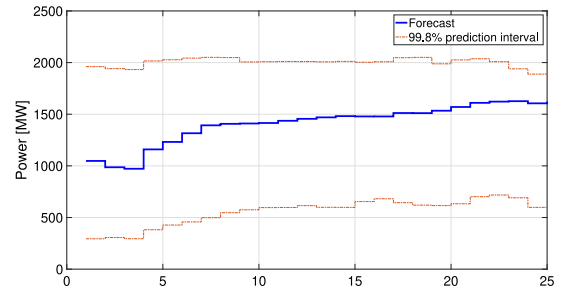


Fig. 9. Aggregated day-ahead wind forecast and 99.8% prediction intervals.

4.2.1. Wind power

Wind production measurements are at a 1-s resolution and coming from two real wind farms with a nominal capacity of 17 MW and 50 MW. Measurements are scaled proportionally to match the capacity of the four wind farms considered in the case study (i.e., 1500 MW, 1200 MW, 750 MW and 600 MW). Forecasts are computed in terms of prediction intervals, which express the range where the realization is predicted to happen at a certain confidence level, and thus are the suitable format to evaluate reserve requirements. For the reasons that will be discussed in 4.3, the target confidence level is 99.8%. Prediction intervals of wind generation are computed with a quantile regression forest model from the existing literature [37,38] trained on historical numerical weather predictions and plant production data. Fig. 9 shows the day-ahead hourly wind forecast and the corresponding prediction intervals at 99.8% confidence level.

4.2.2. Power demand

The active power measurements are adapted from a monitoring system based on PMUs installed in the 125 kV sub-transmission system of Lausanne, Switzerland [39]. Reactive

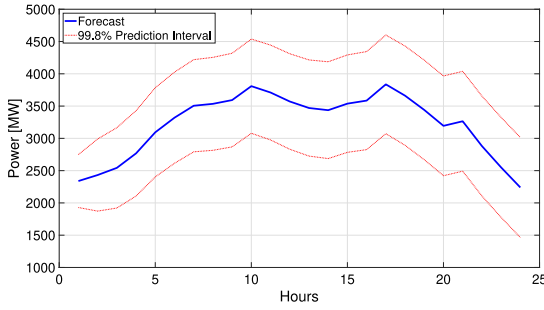


Fig. 10. Aggregated day-ahead demand forecast and 99.8% prediction intervals.

power is computed assuming a constant power factor for the loads. Since the demand level of Lausanne is smaller than the demand level of the IEEE 39-bus benchmark power grid, the measured load profiles are scaled-up to match the rating power of the 19 loads in the 39-bus power grid. Specifically, 7 different demand profiles (i.e., corresponding to measurements at different network buses of Lausanne) and their combinations are used such that the scaled-up profiles for the 19 loads are all different. Forecasting is based on a Seasonal Auto Regression Integrated Moving Average (SARIMA) model with seasonality order of 24 hours, seasonal AR order of 5 (non-zero terms at lags 1, 2, 3 and 5), AR order of 1, MA order of 18 (non-zero terms at lags 1, 6 and 18), and a trend difference order of 1. Fig. 10 shows the day-ahead hourly demand forecast and the corresponding 99.8% prediction intervals.

4.3. System reserves

Power reserves for frequency containment and restoration are calculated referring to the norms of the Swiss national TSO, Swissgrid. Both are allocated as symmetric products and calculated as described next [40,41].

4.3.1. Frequency containment reserve

Typically, national TSOs within a large interconnected system procure reserves for frequency containment proportionally to the size of their systems. Swissgrid, as the Swiss TSO within the electricity grid of continental Europe (UCTE), procures reserve as the pro rata of its maximum load compared to the total UCTE one [42]. Since our low-inertia 39-bus power system is assumed to be non-interconnected, we set the frequency containment reserve as 10% of the peak load, ± 500 MW, using the deterministic notion proposed in [43].

4.3.2. Frequency restoration reserve

ENTSO-E operation handbook recommends attaining zero frequency error with a probability of 99.8% [44]. According to this principle, and since grid imbalances are caused by stochastic generation and demand, we size the power reserve for frequency restoration considering 99.8% prediction intervals of the wind generation and power demand. Fig. 11 shows, in addition to the 99.8% prediction intervals of wind and demand already discussed, the allocated power reserve for frequency restoration. The total positive, R_h^+ (negative, R_h^-), reserve at hour h is the sum of the upper (lower) quantile of the wind and demand prediction intervals. However, since the power reserve is symmetric, the applied total secondary frequency reserve at each hour is $R_h = \pm \max\{|R_h^+|, |R_h^-|\}$.

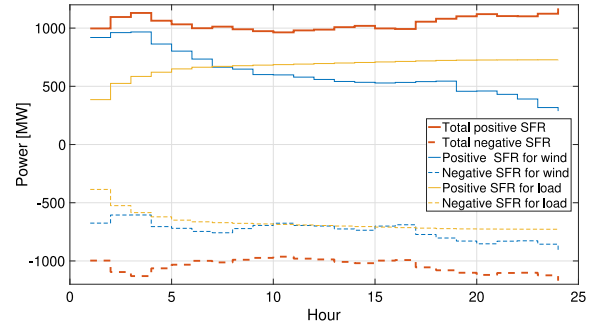


Fig. 11. Secondary frequency reserve for 99.8% prediction intervals.

4.4. Unit commitment for generation and reserve scheduling

We formulate a security constrained unit commitment (SCUC) model for generation and frequency containment and restoration reserves scheduling based on the DC power flow. This model is used as a replace of the day-ahead market set-up to schedule the active power profiles. The BESSs are treated here as an additional frequency regulation service provider. For the sake of a fair comparison in the results section, they are not included in the SCUC (where only synchronous generators are included) because this would determine different operating conditions for the generators, making it difficult to compare the dynamic system performance in the cases with and without the BESS. As a matter of fact, the exclusion of the BESS in the SCUC produces the same boundary conditions on the system allowing to quantify the impact of the BESS on the system dynamics.

The objective is to minimize the economic cost of energy generation and reserve procurement considering the power network constraints, operational (security) constraints, load and renewable energy generation forecast, and reserve requirements. The SCUC model is given in (1). The SCUC model (1) is a mixed integer linear programming problem [45].

$$\text{Minimize } Cost^{uc} = E_{cost} + Up_{cost} + Dw_{cost} + Rev_{cost}$$

subject to

$$E_{cost} = \sum_{n,t} \beta_n p_{gn,t} \quad (1a)$$

$$Up_{cost} = \sum_{n,t} c_{n,t}^{up} u_{n,t}^{up} \quad (1b)$$

$$Dw_{cost} = \sum_{n,t} c_{n,t}^{down} u_{n,t}^{dw} \quad (1c)$$

$$Rev_{cost} = \sum_{n,t} c_{n,t}^{reserve} p_{gn,t}^r \quad (1d)$$

$$p_{gn,t} - p_{dn,t} = \sum_l A(n,l) p_{l,t} + G_n \quad (1e)$$

$$p_{l,t} = \frac{\theta_{sl,t} - \theta_{rl,t}}{X_l} \quad (1f)$$

$$u_{n,t}^{on} Ramp_{n,t}^{dw} \leq p_{gn,t} - p_{gn,t-1} \leq u_{n,t}^{on} Ramp_{n,t}^{up} \quad (1g)$$

$$u_{n,t}^{on} - u_{n,t-1}^{on} = u_{n,t}^{up} - u_{n,t}^{dw} \quad (1h)$$

$$u_{n,t}^{up} + u_{n,t}^{dw} \leq 1 \quad (1i)$$

$$\sum_n p_{gn,t}^r \geq Rev_t \quad (1j)$$

$$u_{n,t}^{on} p_{gn}^{min} \leq p_{gn,t} \leq u_{n,t}^{on} p_{gn}^{max} \quad (1k)$$

$$p_{gn}^{min} \leq p_{gn,t} + p_{gn,t}^r \leq p_{gn}^{max} \quad (1l)$$

$$p_l^{\min} \leq p_{l,t} \leq p_l^{\max} \quad (1m)$$

$$\theta_n^{\min} \leq \theta_n - \theta_{n'} \leq \theta_n^{\max}, \forall n \in N_{PV}, n' \in N_{slack} \quad (1n)$$

$$\theta_l^{\min} \leq \theta_{s,l,t} - \theta_{r,l,t} \leq \theta_l^{\max} \quad (1o)$$

$$\{u_{n,t}^{on}, u_{n,t}^{up}, u_{n,t}^{dw}\} \in \{0, 1\} \quad (1p)$$

The objective cost function $Cost^{uc}$ includes the energy generation cost (linear) E_{cost} , generator start-up cost (linear) Up_{cost} , generator shut-down cost (linear) Dw_{cost} and reserve cost Re_{cost} . $\Omega = \{p_{g,n,t}, u_{n,t}^{on}, u_{n,t}^{up}, u_{n,t}^{dw}\}$ is the set of decision variables. β_n is the cost parameter of energy generation. $C_{n,t}^{up}$, $C_{n,t}^{down}$, $C_{n,t}^{reserve}$ are the cost parameters of generator start-up, shut-down and reserve. $p_{g,n,t}$ is the energy generation of the generator at bus n and time step t . $p_{d,n,t}$ is the active power load forecast. $p_{l,t}$ is the active power flow of transmission line l . $A(n, l)$ is the network matrix with $A(n, l) = 1$ if n is the sending end of transmission line l and $A(n, l) = -1$ if n is the receiving end of transmission line l . G_n is the shunt conductance at bus n . As we are using the DC power flow, the voltage amplitudes are assumed equal to 1 p.u. for all the buses. Constraint (1e) is the active power balance equation. Constraint (1f) is the DC power flow equation. $p_{l,t}$ is the power flow through the transmission line l at time step t . $\theta_{s,l,t}$, $\theta_{r,l,t}$ are the voltage phase angles at the sending end and receiving end of transmission line l . $u_{n,t}^{on}$ is the unit commitment variable. $u_{n,t}^{up}$ is the unit start-up variable. $u_{n,t}^{dw}$ is the unit shut-down variable. Constraint (1g) is the ramp-rate bound. $Ramp_{n,t}^{up}$, $Ramp_{n,t}^{dw}$ are the upper and lower bounds of generators' ramp rates. Constraint (1h) is the relationship among the generator start-up, shut-down and in-operation variables. Constraint (1i) is the bound of start-up and shut-down variables. Constraint (1j) is the requirement of total reserve which is equal to the sum of frequency containment and restoration reserves computed in Section 4.3. Constraint (1k) is the bound for active power generation. Constraint (1l) is the bound of reserve (plus energy generation). Constraint (1m) is the bound of power flow of the transmission line. Constraint (1n) is the phase angle stability bound for all (non-slack bus) generators compared with the slack bus generator. N_{slack} is the set of slack bus generator. N_{PV} is the set of non-slack bus generator. Constraint (1o) is the phase angle bound for all transmission line for security consideration. For the unit commitment variables, $\{u_{n,t}^{on}, u_{n,t}^{up}, u_{n,t}^{dw}\} = 1$ means the generator is in-operation, start-up action and shut-down action, respectively. Otherwise, $\{u_{n,t}^{on}, u_{n,t}^{up}, u_{n,t}^{dw}\} = 0$ means the generator is off-operation, no start-up action or shut-down action.

4.5. Low-inertia IEEE 39-bus power grids

The low-inertia power system considered in this work is derived from the IEEE 39-bus benchmark system, where four synchronous generators (one thermal power plant and three hydro power plants) are replaced with four wind farms. The detailed description of the model is given in [12]. For clarity, its main features are summarized here. The configuration of the low-inertia 39-bus system is shown in Fig. 12. Its inertia constant (referred to a 10 GW base and obtained by summing the inertia constant of all the conventional power plants) has decreased from 7.84 s of the original grid to 1.98 s. Conventional generators are simulated with a sixth-order model for the synchronous generator, a prime mover and governor model [46], and an excitation system associated with an Automatic Voltage Regulator (AVR) [47]. Each wind farm is simulated by scaling up a detailed model of a Type-III wind turbine, including a sixth-order order model for the double-fed induction generator (DFIG) and the averaged model for the AC/DC back-to-back converter [48]. Available power measurements from the wind farms are assumed to be the mechanical power on the turbine shaft. This is done in

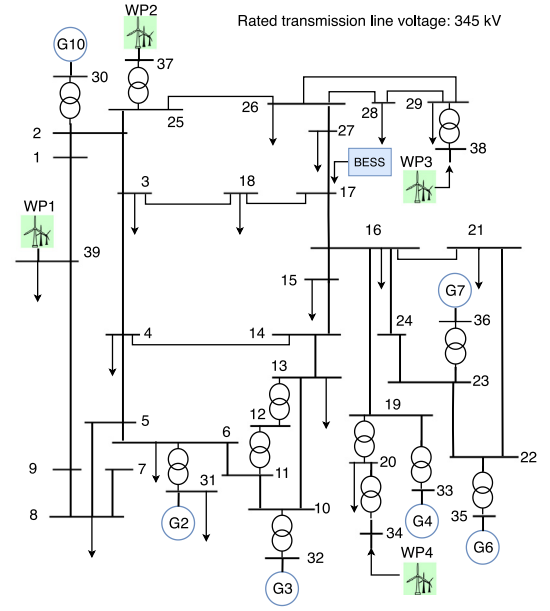


Fig. 12. Diagram of 39-bus low-inertia power systems (The presence of the BESS at bus 17 is taken into account in grid).

order to retain a detailed dynamic modelling representation of interactions among the wind turbines and the power grid. Loads are reproduced with a three-phase frequency and voltage-dependent EPRI LOADSYN load model [49] associated with the input power demand measurements. For the BESS, we consider a single system with a power rating of 225 MVA and energy capacity of 175 MWh. Its model consists of the battery pack and a four-quadrant DC/AC power converter, as shown in Fig. 13. The battery pack is simulated with a three-time-constant equivalent circuit model with SOC-dependent parameters, reported in Table 1. The arrows in the table imply that these values vary linearly with the SOC in the indicated range. We use the model proposed in [50,51] for a Lithium-Titanate-Oxide battery, assuming a 2s156p⁵ configuration of the battery packs (with identical parameters) feeding a single DC bus. The power converter is modelled in detail at the level of the switching devices.

The BESS power rating (approx. 5% of the peak demand) is chosen so as to be of meaningful size for the system. The BESS's energy capacity is chosen as a function of the power rating of the power converter. Commercially available BESSs are commonly designed so that they may be fully charged or discharged in between 30 min to 2 h (according to the C-rate limitations of the cells).

4.6. Case studies

For the purpose of comparison, we test five cases over 24-hour long simulations, where the same generation and reserve schedules obtained from the SCUC are reproduced. Figs. 14(a) and 14(b) show the generation and reserve schedules determined for the day of operations.

Table 2 lists the five cases tested over the 24-hour long simulations. Case 1 is the base configuration with no BESS. Case 2 and Case 3 feature a BESS connected to the low-inertia power grid via a PLL-free grid-forming converter with the p - f droop coefficients of 2% and 1%, corresponding to the f - p control gains of 225 MW/Hz and 450 MW/Hz, respectively. Case 4 and Case 5

⁵ Two battery packs in series, and 156 series in parallel.

Table 1
Parameters of the BESS connected to the HV transmission grid.

SOC[%]	10→30	30→50	50→70	70→90
E [V]	1184.4 → 1250.0	1250.0 → 1305.8	1305.8 → 1360.4	1360.4 → 1466.4
R_s [Ω]	0.052 → 0.042	0.042 → 0.030	0.030 → 0.028	0.028 → 0.026
R_1 [Ω]	0.190 → 0.150	0.150 → 0.180	0.180 → 0.158	0.158 → 0.398
C_1 [F]	4465.0 → 4904.5	4904.5 → 6998.0	6998.0 → 6000.0	6000.0 → 5617.0
R_2 [Ω]	0.080 → 0.018	0.018 → 0.018	0.018 → 0.018	0.018 → 0.020
C_2 [F]	454.50 → 1069.5	1069.5 → 1241.0	1241.0 → 1245.0	1245.0 → 1252.5
R_3 [Ω]	5.0e−3 → 9.8e−5	9.8e−5 → 4.8e−4	4.80e−4 → 13.6e−4	13.6e−4 → 12.0e−4
C_3 [F]	272.10 → 394.50	394.50 → 1479.8	1479.8 → 2250.0	2250.0 → 3088.7

Table 2

Cases studied through day-long simulations.

Case	BESS converter control	f - p Gain
Case 1	No BESS	–
Case 2	Grid-forming	225 MW/Hz
Case 3	Grid-forming	450 MW/Hz
Case 4	Grid-following with supporting mode	225 MW/Hz
Case 5	Grid-following with supporting mode	450 MW/Hz

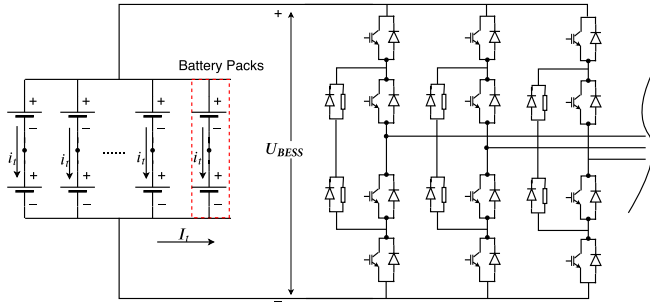


Fig. 13. Diagram of BESS-VSC.

are the two cases where the BESS is connected to the low-inertia power grid through a grid-following converter with f - p control gains of 225 MW/Hz and 450 MW/Hz, respectively. For the sake of brevity, in the following of this section we also use f - p control gains for the grid-forming converter.

5. Results

5.1. Metrics

In order to quantitatively evaluate the frequency containment, the following metrics are used.

- Frequency Probability Density Function (PDF), identified using the 24-hour frequency measurements from the 19 simulated PMUs (with a reporting rate of 50 frames per second) located at 19 load buses [52].
- Integral Frequency Deviation (IFD):

$$IFD = \sum_{i=1}^L \sum_{k=1}^N |f_{k,i} - f_0| \quad (2)$$

where L is the number of loads and N is the total sampling number of frequency measurements for each load.

- Relative Rate-of-Change-of-Frequency (rRoCoF):

$$rRoCoF = \frac{\Delta f_{pcc} / \Delta t}{\Delta P_{BESS}} \quad (3)$$

where Δf_{pcc} is the difference between one grid frequency sample and the next (once-differentiated value) at the bus where the BESS is connected to, ΔP_{BESS} is the once-differentiated BESS active power, and Δt is the sampling interval.

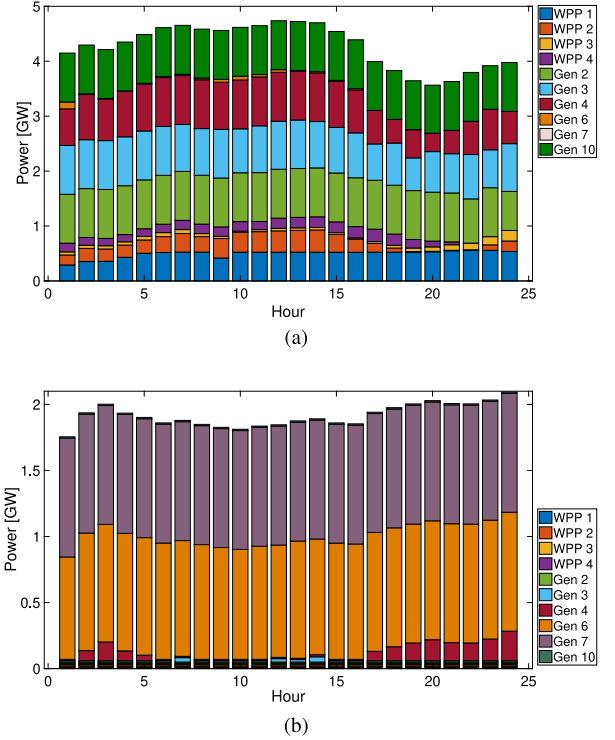


Fig. 14. Generation and reserve schedules. Generation schedule (a); Frequency containment and restoration reserve schedule (b).

The frequency PDF and IFD measure grid frequency deviations from the nominal value and are used to assess frequency containment performance. The rRoCoF measures the RoCoF regulation at PCC weighted by the delivered active power of the BESS and is used to compare the performance of grid-forming versus grid-following converters.

5.2. Results and discussions

This section presents and discusses the simulation results for the 5 cases listed in Table 2. Fig. 15(a) shows the system frequency for the 5 cases. In the zoomed region, we show the grid frequency dynamics at the beginning of the 15-th hour, where a considerable frequency deviation happens. The cases with a higher f - p control gain attain more frequency containment because of the larger regulating power provided, as visible in the zoomed region of Fig. 15(b). While Fig. 15 provides a general view of the system frequency responses, the defined metrics allow a better scrutiny of the control performance and will be described next.

5.2.1. IFD

The IFD results in Table 3 shows that the case without BESS (i.e., Case 1) scores the highest IFD. In Case 2 and Case 3, IFD

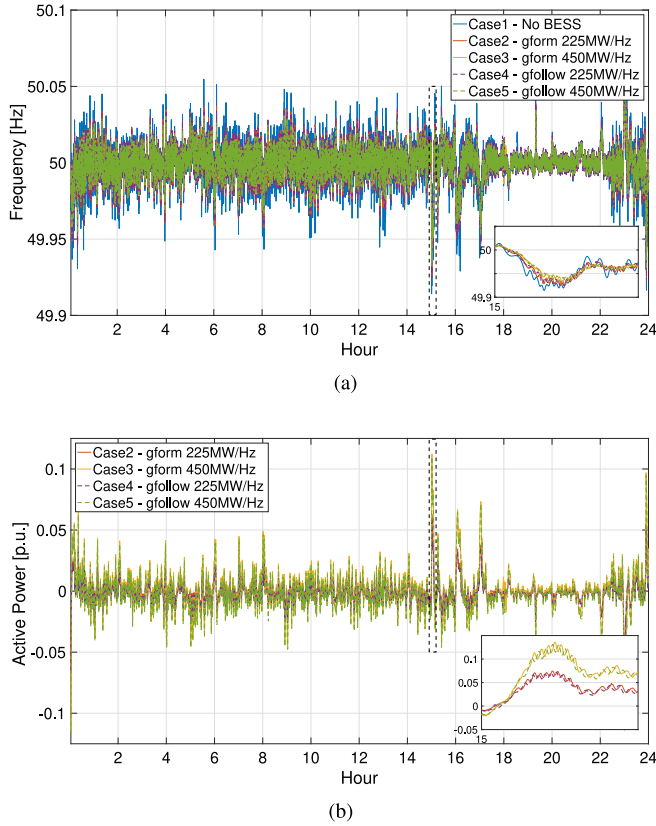


Fig. 15. System frequency and BESS active power. System frequency (represented by the rotor speed of Generator 2) (a); BESS active power (b).

Table 3
Integrated Frequency Deviation and apparent power for the 5 cases.

Case	IFD [Hz]	$\sum S_{BESS}$ [MVA-h]
Case 1	7.547×10^5	–
Case 2	6.718×10^5	435.5
Case 3	6.015×10^5	442.8
Case 4	6.798×10^5	558.3
Case 5	6.138×10^5	564.3

decreases by 11.0% and 20.3%, respectively, compared to Case 1. In Case 4 and Case 5, IFD decreases by 10.0% and 18.7%, respectively. This is in accordance with the expectation that the higher f - p control gain (i.e., 450 MW/Hz) provides more frequency containment, therefore reducing deviations of the grid frequency.

5.2.2. PDF

Fig. 16 shows the PDF estimated from the frequency measurements on the 19 loads. The PDF results are consistent with the value of IFD, demonstrating that the higher control gain results in smaller standard deviation and higher probability at 50 Hz. By comparing Case 2 and Case 4, the two cases with the lowest f - p control gain, we can observe that the grid-forming and grid-following converters achieve an equivalent increment of performance for frequency containment. After examining the values of IFD and PDF standard deviation for Case 3 and Case 5, we can observe that, for a higher f - p control gain, the grid-forming converter performs better than the grid-following converter, achieving a 2% reduction of IFD and 1% reduction of PDF standard deviation.

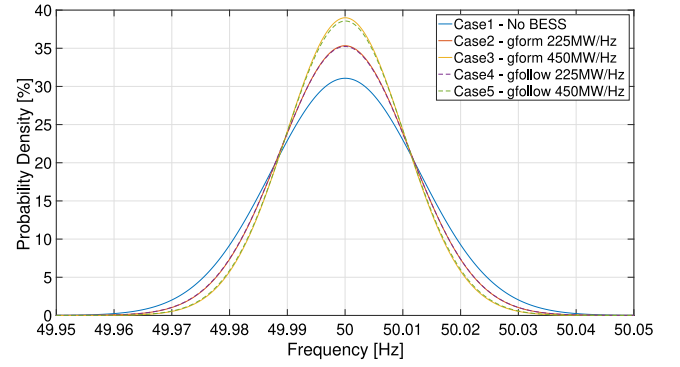


Fig. 16. Probability density function for frequency measurements of 19 loads. Standard deviation for each case: $\sigma_{case1}^f = 0.0128$, $\sigma_{case2}^f = 0.0113$, $\sigma_{case3}^f = 0.0102$, $\sigma_{case4}^f = 0.0113$, and $\sigma_{case5}^f = 0.0103$.

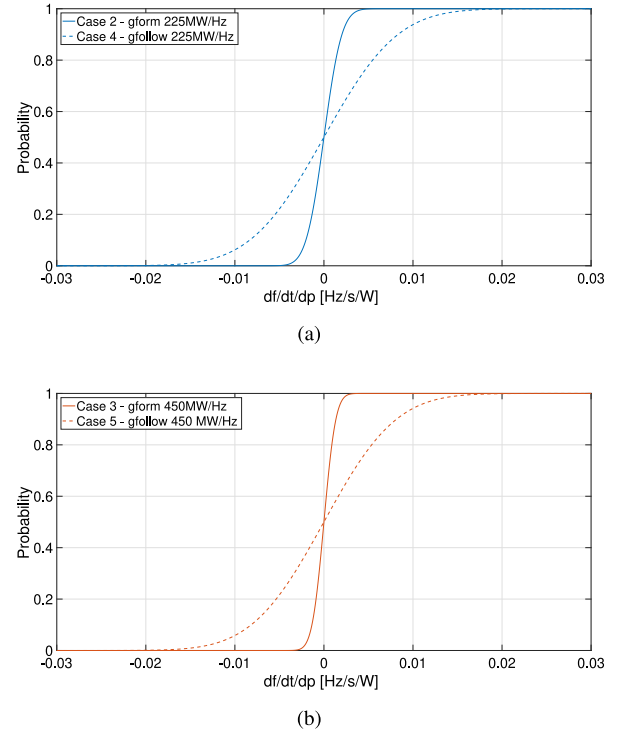


Fig. 17. Cumulative density function (CDF) of rRoCoF. Case2 and Case4 (a); Case3 and Case5 (b).

5.2.3. rRoCoF

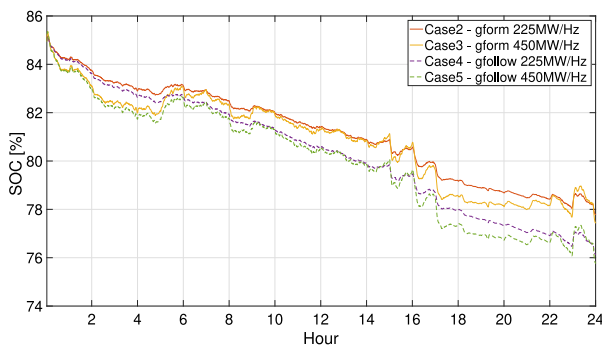
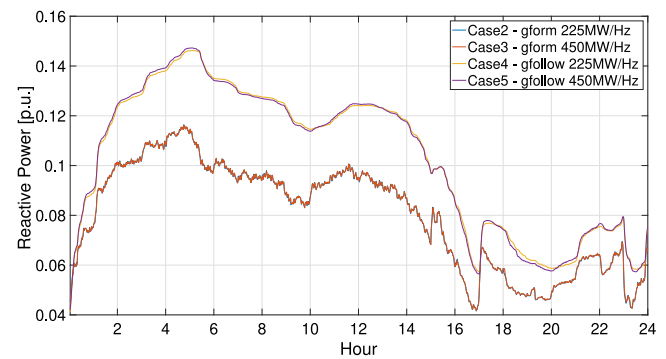
Fig. 17 illustrates the Cumulative Density Functions (CDFs) of rRoCoF for the larger and smaller f - p gains for both grid-forming and grid-following converter. For the smaller gain in Fig. 17(a), the grid-forming converter performs better than the grid-following converter as it achieves lower RoCoF per Watt of regulating power. The standard deviation of rRoCoF for Case 2 and 4 are $\sigma_{case2}^{rRoCoF} = 0.0016$ and $\sigma_{case4}^{rRoCoF} = 0.0065$, respectively. Fig. 17(b) shows that also for the larger gain, the grid-forming converter performs better than the grid-following as it achieves smaller frequency rates. In this case, the corresponding standard deviations of rRoCoF are $\sigma_{case3}^{rRoCoF} = 0.0013$ and $\sigma_{case5}^{rRoCoF} = 0.0064$ for Case 3 and 5, respectively.

Fig. 18 shows the evolution in time of the BESS state of charge (SOC). It is interesting to observe its decreasing trend, that, since the average grid frequency along the day is 50 Hz due to the frequency restoration action, is to ascribe to power losses on the

Table 4

List of parameters in the frequency controls of the Low-inertia 39-bus Power grid.

Grid-forming control		Grid-following control		Frequency control of synchronous generators	
m_p	2%/1%	$K_{f-p}^{following}$ [MW/Hz]	225/450	R_p	5%
				T_s [s]	120
				k_a	1
				T_a [s]	0.2
n_q [V/MVar]	0.33	$K_{v-q}^{following}$ [MVar/V]	1.5	$k_{p,gov}$	2.4
		ΔV_{tr} [p.u.]	± 0.005	G2	0.36
				G3	0.30
				G4	0.39
ω_{LP} [rad/s]	31.4	ω_{LF} [rad/s]	157	$k_{i,gov}$	0.31
				G6	0.41
				G7	0.26
				G10	0.26
T_1 [s]	0.0333	$k_{p,pll}$	60	G2	2.02
				G3	2.39
				G4	1.90
T_2 [s]	0.0111	$k_{i,pll}$	1400	G6	2.32
				G7	1.76
				G10	2.80

**Fig. 18.** Evolution in time of the battery state of charge.**Fig. 19.** BESS reactive power.

AC- and DC-side filters. Thanks to the high fidelity of the dynamic models, we are capable to numerically quantify the impact of converter controls on the SOC evolution. Since the energy losses are proportional to the apparent power $S_{BESS} = \sqrt{P_{BESS}^2 + Q_{BESS}^2}$, Table 3 reports the integral of the BESS apparent power over the 24 h of the simulation.

On one hand, the PDF of frequency (therefore the active power of BESS) is more dependent on the droop setting. As we compare Case 3 vs Case 2 or Case 5 vs Case 4, we do observe that the cases with the high control gain 450 MW/Hz correspond to higher apparent power due to converter's higher active power output than in the cases with the low control gain 225 MW/Hz. Therefore, for the same control law, we observe a larger SOC decrease in the case with higher control gain.

On the other hand, the grid-following unit exhibits a higher apparent power throughput than in the case of grid-forming unit due to its converter's higher reactive power output, as shown in Fig. 19. The grid-following converter provides higher reactive power because of its voltage-reactive power (v-q) regulator, which supports the grid voltage by injecting reactive power as the grid-voltage varies. Conversely, the grid-forming unit adjusts the converter's voltage magnitude to limit the reactive power deviation from its reference value, therefore reducing the impact of grid voltage variation on the reactive power exchange.

6. Conclusions

In this paper, the full-replica dynamic model of the low-inertia 39-bus power grid has been used to assess the performance of

grid-forming and grid-following converter-interfaced BESS in enhancing frequency containment regulation. In order to reproduce a real operational scenario, frequency containment and restoration reserves are allocated with the same margins and procedures adopted by TSOs nowadays. To this end, a SCUC problem embedding prediction intervals from real forecasters of wind generation and electric demand is formulated. Based on the SCUC schedule, we run 24-hour long dynamic simulations reproducing the real outcome of the stochastic wind generation and demand (both from high-resolution measurements at a 1-s resolution). In the simulations, we compare the performance of 5 cases: no BESS, BESS with grid-forming converter small (225 MW/Hz) and large (445 MW/Hz) f - p gains, and BESS with grid-following converter with same gains.

The results quantitatively verified, by means of suitably-defined frequency metrics, that the grid-forming control strategy outperforms the grid-following one achieving better frequency containment and lower relative RoCoF. Simulations also quantitatively demonstrate that large-scale BESSs are capable of significantly improving the system frequency containment, and the level of improvement is proportionally related to the level of f - p gain.

CRedit authorship contribution statement

Yihui Zuo: Methodology, Software, Validation, Formal analysis, Writing - original draft, Visualization. **Zhao Yuan:** Methodology, Data curation, Writing - review & editing. **Fabrizio Sossan:** Methodology, Resources, Supervision, Writing - review & editing. **Antonio Zecchino:** Formal analysis, Writing - review & editing.

Rachid Cherkaoui: Conceptualization, Writing - review & editing.
Mario Paolone: Conceptualization, Supervision, Writing - review & editing, Resources, Project administration.

Declaration of competing interest

The authors declare that they have no known competing financial interests or personal relationships that could have appeared to influence the work reported in this paper.

Appendix

Table 4 lists the values of the parameters in the frequency controls that are applied in the low-inertia -39 bus power grid.

References

- [1] A.Z. Amin, Renewable Energy Prospects for the European Union, Tech. Rep., IRENA and European Commission, 2018.
- [2] AEMO, Review of the Black System South Australia Report – System Event of 28 September 2016, Tech. Rep., AEMO, 2017.
- [3] Y. Sun, S.V. Wachche, A. Mills, O. Ma, 2018 Renewable Energy Grid Integration Data Book, Tech. Rep., National Renewable Energy Lab.(NREL), Golden, CO (United States), 2020.
- [4] AEMO, Renewable Integration Study: Stage 1 Report, Tech. Rep., AEMO, 2020.
- [5] CAISO, Frequency Response Phase 2, Tech Rep, CAISO, 2016.
- [6] A. Zecchino, Z. Yuan, F. Sossan, R. Cherkaoui, M. Paolone, Optimal provision of concurrent primary frequency and local voltage control from a BESS considering variable capability curves: Modelling and experimental assessment, *Electr. Power Syst. Res.* 190 (2021) 106643.
- [7] B. Dunn, H. Kamath, J.-M. Tarascon, Electrical energy storage for the grid: A battery of choices, *Science* 334 (6058) (2011) 928–935.
- [8] AEMO, Initial operation of the Hornsdale Power Reserve Battery Energy Storage System, Technical Report, 2018.
- [9] VISTRA Energy, 2018 Sustainability Report, Tech. Rep., 2018.
- [10] P.V. Brogan, R.J. Best, D.J. Morrow, K. McKinley, M.L. Kubik, Effect of BESS response on frequency and RoCoF during underfrequency transients, *IEEE Trans. Power Syst.* 34 (1) (2019) 575–583.
- [11] U. Datta, A. Kalam, J. Shi, The relevance of large-scale battery energy storage (BES) application in providing primary frequency control with increased wind energy penetration, *J. Energy Storage* 23 (2019) 9–18.
- [12] Y. Zuo, M. Paolone, F. Sossan, Effect of voltage source converters with electrochemical storage systems on dynamics of reduced-inertia bulk power grids, *Electr. Power Syst. Res.* 189 (2020) 106766.
- [13] M. Paolone, A. Monti, T. Gaunt, T. Van Cutsem, X. Guillaud, V. Vittal, M. Liserre, C. Vournas, S. Meliopoulos, Fundamentals of power systems modelling in the presence of converter-interfaced generation, in: 21st PSCC, 2020.
- [14] A. Mehri-Sani, R. Iravani, Potential-function based control of a microgrid in islanded and grid-connected modes, *IEEE Trans. Power Syst.* 25 (4) (2010) 1883–1891.
- [15] J. Rocabert, A. Luna, F. Blaabjerg, P. Rodríguez, Control of power converters in AC microgrids, *IEEE Trans. Power Electron.* 27 (11) (2012) 4734–4749.
- [16] T. Qoria, E. Rokrok, A. Bruyere, B. François, X. Guillaud, A PLL-free grid-forming control with decoupled functionalities for high-power transmission system applications, *IEEE Access* 8 (2020) 197363–197378.
- [17] P. Unruh, M. Nuschke, P. Strauß, F. Welck, Overview on grid-forming inverter control methods, *Energies* 13 (10) (2020).
- [18] J. Matevosyan, B. Badrzadeh, T. Prevost, E. Quitmann, D. Ramasubramanian, H. Urdal, S. Achilles, J. MacDowell, S.H. Huang, V. Vital, J. O'Sullivan, R. Quint, Grid-forming inverters: Are they the key for high renewable penetration? *IEEE Power Energy Mag.* 17 (6) (2019) 89–98.
- [19] J. Driesen, K. Visscher, Virtual synchronous generators, in: 2008 IEEE Power and Energy Society General Meeting - Conversion and Delivery of Electrical Energy in the 21st Century, 2008, pp. 1–3.
- [20] J. Liu, Y. Miura, T. Ise, Comparison of dynamic characteristics between virtual synchronous generator and droop control in inverter-based distributed generators, *IEEE Trans. Power Electron.* 31 (5) (2016) 3600–3611.
- [21] B. Li, L. Zhou, Power decoupling method based on the diagonal compensating matrix for VSG-controlled parallel inverters in the microgrid, *Energies* 10 (12) (2017).
- [22] H. Beck, R. Hesse, Virtual synchronous machine, in: 2007 9th International Conference on Electrical Power Quality and Utilisation, 2007, pp. 1–6.
- [23] M. Yu, A.J. Roscoe, C.D. Booth, A. Dysko, R. Ierna, J. Zhu, N. Grid, H. Urdal, Use of an inertia-less Virtual Synchronous Machine within future power networks with high penetrations of converters, in: 2016 Power Systems Computation Conference, PSCC, 2016, pp. 1–7.
- [24] Y. Chen, R. Hesse, D. Turschner, H. Beck, Improving the grid power quality using virtual synchronous machines, in: 2011 International Conference on Power Engineering, Energy and Electrical Drives, 2011, pp. 1–6.
- [25] Q. Zhong, G. Weiss, Synchronverters: Inverters that mimic synchronous generators, *IEEE Trans. Ind. Electron.* 58 (4) (2011) 1259–1267.
- [26] R. Rosso, S. Engelken, M. Liserre, Robust stability analysis of synchronverters operating in parallel, *IEEE Trans. Power Electron.* 34 (11) (2019) 11309–11319.
- [27] M. Guerrero, L.G. de Vicuna, J. Matas, M. Castilla, J. Miret, A wireless controller to enhance dynamic performance of parallel inverters in distributed generation systems, *IEEE Trans. Power Electron.* 19 (5) (2004) 1205–1213.
- [28] Q. Taoufik, C. Quentin, L. Chuanyue, G. Xavier, C. Frederic, G. François, K. Xavier, Deliverable 3.2: Local control and simulation tools for large transmission systems, in: MIGRATE Project, 2018.
- [29] E. Rokrok, T. Qoria, A. Bruyere, B. François, X. Guillaud, Classification and dynamic assessment of droop-based grid-forming control schemes: Application in HVDC systems, *Electr. Power Syst. Res.* 189 (2020) 106765.
- [30] D. Raisz, T.T. Thai, A. Monti, Power control of virtual oscillator controlled inverters in grid-connected mode, *IEEE Trans. Power Electron.* 34 (6) (2019) 5916–5926.
- [31] T.T. Thai, D. Raisz, A. Monti, F. Ponci, A. Ahmadifar, Voltage harmonic reduction using virtual oscillator based inverters in islanded microgrids, in: 2018 18th International Conference on Harmonics and Quality of Power, ICHQP, 2018, pp. 1–6.
- [32] G. Denis, T. Prevost, P. Panciatici, X. Kestelyn, F. Colas, X. Guillaud, Improving robustness against grid stiffness, with internal control of an AC voltage-controlled VSC, in: IEEE PESGM, 2016, pp. 1–5.
- [33] S. Golestan, J.M. Guerrero, J.C. Vasquez, Three-phase PLLs: A review of recent advances, *IEEE Trans. Power Electron.* 32 (3) (2017) 1894–1907.
- [34] S. Golestan, M. Ramezani, J.M. Guerrero, F.D. Freijedo, M. Monfared, Moving average filter based phase-locked loops: Performance analysis and design guidelines, *IEEE Trans. Power Electron.* 29 (6) (2014) 2750–2763.
- [35] P.S.D.P. Committee, et al., Dynamic models for turbine-governors in power system studies, *IEEE Power Energy Soc.* (2013).
- [36] DESL-EPFL, Extension of the IEEE 39-bus test network for the study of fundamental dynamics of modern power system, 2019, (Online). Available: <https://github.com/DESL-EPFL>.
- [37] S. Camal, A. Michiorri, G. Kariniotakis, Optimal offer of automatic frequency restoration reserve from a combined PV/Wind virtual power plant, *IEEE Trans. Power Syst.* 33 (6) (2018) 6155–6170.
- [38] S. Camal, A. Michiorri, G. Kariniotakis, Forecasting extremes of aggregated production from a RES virtual power plant, in: Proceedings of the Wind Energy Science Conference 2019, EAWC - European Academy of Wind Energy, Cork, Ireland, 2019, (Online). Available: <https://hal.archives-ouvertes.fr/hal-02158589>.
- [39] L. Zanni, A. Derviškić, M. Pignati, C. Xu, P. Romano, R. Cherkaoui, A. Abur, M. Paolone, PMU-based linear state estimation of lausanne subtransmission network: Experimental validation, in: 21st PSCC, 2020.
- [40] F. Abbaspourtorbati, M. Zima, The Swiss reserve market: Stochastic programming in practice, *IEEE Trans. Power Syst.* 31 (2) (2016) 1188–1194.
- [41] J. Abrell, The Swiss Wholesale Electricity Market, Tech. Rep., Swiss Competence Center for Energy Research, 2016.
- [42] ENTSO-E, Continental Europe Operation Handbook, Tech. Rep., OpHB-Team, 2016.
- [43] A.A. Khatir, R. Cherkaoui, M. Zima, Literature survey on fundamental issues of frequency control reserve (FCR) provision, *Swiss Electr. Res.* (2010).
- [44] ENTSO-E, Policy 1 – Load-Frequency Control and Performance, Tech. Rep., UCTE Operation Handbook, OpHB-Team, 2016.
- [45] Z. Yuan, M. Paolone, Properties of convex optimal power flow model based on power loss relaxation, *Electr. Power Syst. Res.* 186 (2020) 106414.
- [46] Dynamic models for steam and hydro turbines in power system studies, *IEEE Trans. Power Appar. Syst.* (6) (1973) 1904–1915.
- [47] IEEE draft recommended practice for excitation system models for power system stability studies, 2015, pp. 1–202, IEEE P421.5/D38.
- [48] R. Pena, J.C. Clare, G.M. Asher, Doubly fed induction generator using back-to-back PWM converters and its application to variable-speed wind-energy generation, *IEE Proc. – Electr. Power Appl.* 143 (3) (1996) 231–241.
- [49] Load representation for dynamic performance analysis (of power systems), *IEEE Trans. Power Syst.* 8 (2) (1993) 472–482.
- [50] F. Sossan, E. Namor, R. Cherkaoui, M. Paolone, Achieving the dispatchability of distribution feeders through prosumers data driven forecasting and model predictive control of electrochemical storage, *IEEE Trans. Sustain. Energy* 7 (4) (2016) 1762–1777.
- [51] E. Namor, F. Sossan, E. Scolari, R. Cherkaoui, M. Paolone, Experimental assessment of the prediction performance of dynamic equivalent circuit models of grid-connected battery energy storage systems, in: IEEE ISGT, 2018.
- [52] P. Romano, M. Pignati, M. Paolone, Integration of an IEEE Std. C37.118 compliant PMU into a real-time simulator, in: 2015 IEEE Eindhoven PowerTech, 2015, pp. 1–6.